

A deep learning approach to multi-track location and orientation in gaseous drift chambers

Pengcheng Ai^a, Dong Wang^a, Xiangming Sun^{a,*}, Guangming Huang^{a,*}, Zili Li^a

^a*Central China Normal University, No.152 Luoyu Road, Wuhan, Hubei, 430079
P.R.China*

Abstract

Accurate measuring the location and orientation of individual particles in a beam monitoring system is of particular interest to researchers in multiple disciplines. Among feasible methods, gaseous drift chambers with hybrid pixel sensors have the great potential to realize long-term stable measurement with considerable precision. In this paper, we introduce deep learning to analyze patterns in the beam projection image to facilitate three-dimensional reconstruction of particle tracks. We propose an end-to-end neural network based on segmentation and fitting for feature extraction and regression. Two segmentation heads, named binary segmentation and semantic segmentation, perform initial track determination and pixel-track association. Then pixels are assigned to multiple tracks, and a weighted least squares fitting is implemented with full back-propagation. Besides, we introduce a center-angle measure to judge the precision of location and orientation by combining two separate factors. The initial position resolution could achieve $8.8 \mu m$ for the single track and $11.4 \mu m$ ($15.2 \mu m$) for the 1-3 tracks (1-5 tracks), and the angle resolution could achieve 0.15° and 0.21° (0.29°) respectively. These results show a significant improvement in accuracy and multi-track compatibility compared to traditional methods.

Keywords: Multi-track location and orientation, Pixel sensors, Gaseous drift chambers, Convolutional neural networks, Deep learning, Image segmentation, Weighted least squares fitting

*Corresponding authors

Email addresses: `sphy2007@126.com` (Xiangming Sun), `gmhuang@mail.ccnu.edu.cn` (Guangming Huang)

1. Introduction

In the context of high energy physics, the *beam physics* studies the characteristics of particles with similar position and momentum under the electromagnetic fields. The charged particles range from electrons, positrons, protons to some medium-weight or heavy ions. To accelerate the charged particles to relatively high energy, synchrotrons with alternative electric fields and gradually increased magnetic fields are constructed to force the particles to speed up and deflect. Particle beams are widely used in many applied and experimental domains. For example, in semiconductor industry, ions are accelerated to stop and implant into the substrate; in radiation medicine, hadrons are focused onto the pathological tissues; in high energy physics experiments, particles with extremely high energy are collided and observed, and so on.

Under many circumstances, measuring the information (position, angle) of individual particles in a beam with high precision has great significance. For example, in large-scale accelerator equipment [1], the initial beam undergoes multiple manipulations and its profile becomes very complicated, so it is necessary to accurately measure the particles in the beam. Another example is the hadron therapy [2] intensely researched in recent years. In order to focus the beam at the location of tumor and form the Bragg Peak [3], online monitoring the location and orientation of the beam is vital to avoid damaging the normal body. According to different applications, the required precision of the position varies from millimeter-scale to micrometer-scale.

Based on different detection principles, there are several methods to accurately determine the information of the beam. In [4] and [5], parallel-plate ionization chambers and strip electrodes were used to measure the ionization charges induced by the incoming particle so as to measure the incident location. Besides, diamond sensors [6] using the chemical vapor deposition were radiation hardened and had high electron and hole mobility, which could be used for beam measurement in extreme environments. In [7], array structures made up of the scintillator and photo multiplier tubes (or silicon photo multipliers) could realize measurement with high timing resolution and medium spatial resolution. Finally, in [8], fiber optic radiation sensors transmitting fluorescent light were arranged in a grid to achieve sub-millimeter precision of spatial resolution.

Apart from above methods, silicon-based pixel sensors featuring excellent spatial and timing resolution, rapid response and flexible readout are good candidates in the scenario of beam monitoring. According to the relative location between the pixel sensor and the beam, the detection methods can be divided into two types: *targeting* and *drifting*. The *targeting* type places the pixel sensor facing the incoming beam. The particles in the beam penetrate the pixel sensor and generate charges collected by the electrodes [9]. Generally, the *targeting* type has rigorous demands on the radiation hardening, and in most cases the incoming particles are light-weighted, because the deposition of heavy ions will cause the malfunction of the sensor. Relatively speaking, the *drifting* type utilizes the ionization of beam particles in the gaseous chamber, and an electric field vertical to beam direction is imposed. Under the electrostatic force, ionization charges reach the pixel sensor on the detecting plane. The sensor only receives the drifting charges and measures the track of beam particles indirectly. Because the sensor is placed parallel to the beam direction, high energy particles will not run across the sensor. Hence, the radiation damage to the sensor is negligible, and there is no limitation on the kind of particles, as long as the ionization is significant enough to be detected. However, the charge cloud will diffuse in transverse (parallel to the pixel sensor) and longitudinal (vertical to the pixel sensor) directions. How to tackle the diffusion and improve spatial and timing resolution is a main issue for the *drifting* type.

In such a measuring system based on the gaseous drift chamber and the pixel sensor, enabling multi-track location and orientation has a lot of merits (discussed in Section 2). In order to obtain the ability, we need to intelligently figure out the presented tracks from an image generated by the pixel sensor, and output the per-track information. The procedure can be divided into the step of segmentation and the step of regression. Regarding the segmentation problem, much progress has been achieved in recent years because of the renowned *deep learning* [10] techniques. Some representative examples include: the Fully Convolutional Network [11] replaced the traditional fully connected layers with convolution layers, and used up-sampling to get pixel-level classification results; SegNet [12] constructed the encoder-decoder architecture and mapped the index of pooling in the encoder layers to corresponding decoder layers; ENet [13] worked based on the former two structures, and achieved similar results with less parameters; recently, LaneNet [14] adopted the overall architecture from ENet, and used instance segmentation to assist clustering before curve fitting.

In this paper, we present a deep learning architecture to analyze the particular patterns of ionization track projections acquired from the pixel sensor. It is the most important process to reconstruct the three-dimensional (3D) track and get its location and orientation. The main contributions are listed as follows:

- We create an end-to-end neural network based on segmentation and fitting. The base network takes the encoder-decoder architecture, and the *binary segmentation* head and the *semantic segmentation* head are built upon the base network. The network can effectively extract features from the raw track image, and facilitate subsequent operations.
- We invent a pixel assignment algorithm to assign the pixels on the heat-map to multiple tracks. The pixel assignment combines the results from two heads, and pave the way for subsequent weighted least squares fitting.
- We implement the weighted least squares fitting in the software framework of deep learning. The whole network can be optimized end-to-end through back-propagation, and we show the improvement of performance by finetuning the network in an end-to-end way.
- To evaluate the results, we propose a *center-angle measure* (CAM) which combines the information from both the location regression and the angle regression. Based on this measure, we investigate the detection rate (for the single track) and F1-scores (for multiple tracks) versus the CAM threshold.
- Finally, to demonstrate the practicality of the method, we apply the neural network model to experimental images. The results show the correctness of the simulation process and confirm the same model can generalize to experimental data.

2. Multi-Track Measuring System

Since 2012, the *Topmetal* series [15, 16, 17] have been researched and developed for beam monitoring applications. The *Topmetal* is a hybrid pixel sensor with position and amplitude resolution. It features ultra low noise level (equivalent noise charge less than 15 electrons) and high charge sensitivity (10-100 $\mu\text{V}/\text{electron}$). Around 2016, we performed the beam test using

carbon ions with 80.55 MeV/u (mega electron volt per nucleon) energy at Heavy Ion Research Facility in Lanzhou (HIRFL). With the array structure of *Topmetal-II*-, the spatial resolution was better than 20 μm and the angle resolution was better than 0.5° [2]. Around 2019, the same pixel sensor was tested using krypton ions with 25 MeV/u at HIRFL. After pre-selection of images, better results were achieved (4 μm and 0.15°) [18]. Based on the former experiences, we plan to develop new *Topmetal* chips for the Cooler Storage Ring External Target Facility Experiment (CEE). The following two sub-sections will discuss the necessity for multi-track measuring and introduce the proposed multi-track measuring system.

2.1. Necessity for Multi-Track Measuring

The original beam monitoring system [18] was designed to locate single-event latchups of the device under test (DUT). The instrument is the same as Figure 2, except for the time sensitive region which is not present on *Topmetal-II*-. The locating system is comprised of two independent gaseous drift chambers, each of which is filled with air at 1 atm. The pixel sensor works as the anode (0 V), and the face-to-face metal board works as the cathode (-500 V). The DUT is placed on the right side of the second drift chamber. When an ion with relatively high energy passes through the detecting instrument, it will collide with gas molecules and leave a track of electron-positive ion pairs. Under the effect of the electric field, the electrons move towards the pixel sensor anode, and positive ions move towards the metal board cathode. The ionization electrons are collected by the pixel electrodes. Charge signals are read out line by line and pixel by pixel at a working frequency (1.5625 MHz). Finally, track projection images with a fixed refreshing rate (3.3 ms) are sent to and processed by the computer.

Strip-like patterns will appear on the track projection images (dark yellow regions in Figure 2). The width of the strip is determined by the diffusion coefficients and the drifting distance. Usually the energy of the incoming ion is high enough so that colliding with gas molecules has a minor effect on its direction. If we assume the electric field is uniform and the ionization charges are distributed ideally, the center line of the strip can represent the direct projection of traversing path of the ion. One projection line can determine a plane perpendicular to the pixel sensor anode; two such planes have an intersecting line, which can be regarded as the traversing path of the ion.

We performed beam test with krypton ions at HIRFL. A photograph of the testing scene is shown in Figure 1. The flux ranged from 10 ions/($\text{cm}^2\cdot\text{s}$)



Figure 1: The photograph of the former beam test at HIRFL with the gaseous drift chambers and the *Topmetal* pixel sensor.

to 1.5×10^4 ions/(cm²·s). When operating at a low flux, most images from the pixel sensor were empty with background noise, and a few had a single projection track; increasing flux would result in more images with a single track, and images with two or more tracks started to appear (pile-up); when we continued to increase the flux, pile-ups became prevalent; at a very high flux, substantial pile-ups would make individual tracks unrecognizable.

Table 1: The relation between the quantile of the Poisson distribution and the distribution parameter λ at different detection rates. Probability distribution function: $f(k) = \exp(-\lambda)\lambda^k/(k!)$

Quantile	95% detection		97% detection		99% detection	
	λ	rate	λ	rate	λ	rate
k=1	0.3554	1.00	0.2676	1.00	0.1486	1.00
k=2	0.8177	2.30	0.6649	2.48	0.4361	2.93
k=3	1.3664	3.84	1.1551	4.32	0.8233	5.54
k=4	1.9702	5.54	1.7061	6.38	1.2792	8.61
k=5	2.6131	7.35	2.3005	8.60	1.7853	12.01

According to the above observations, the capability to accurately analyze the track information, especially in pile-up situations, is of great importance

to improve the efficiency of the detecting instrument. Some empirical methods could very well determine the single track information. To avoid losing valuable events when the pile-up happens, the system must operate at a relatively low flux. This will inevitably prolong the time needed to reach the required dose of radiation. On the other hand, if we could locate and orient multiple tracks when they are recognizable, the flux might increase significantly at the same detection rate. Assuming the incoming ions in a unit of time obey the Poisson distribution, we could argue that the distribution parameter λ is proportional to the flux. Table 1 shows the relation between the quantile and distribution parameter λ at different detection rates. It can be seen that when the detection rate is fixed, λ will increase with respect to the increase of the quantile, and the tendency gradually becomes speeding up. This phenomenon is more obvious at high detection rates. We might take the first line and the third line in the table as an example. When the detection rates are 95%, 97%, 99%, the λ values when $k=3$ are 3.84, 4.32, 5.54 times bigger than those when $k=1$. It demonstrates that increasing recognizable pile-ups will make it possible for the system to work at higher fluxes. Meanwhile, the decrease of empty background images could also improve the efficiency of the data transmission back-end.

2.2. Multi-Track Measuring System

In Section 2.1, we introduce the detecting instrument with an emphasis on the necessity to measure multiple tracks. However, we do not settle the issue of ambiguity when reconstructing the 3D track from coordinate plane projections. Since each track projection could determine a perpendicular plane, if there are several tracks projecting on the two coordinate planes (assuming n tracks), the reconstructed 3D tracks have more than one possibility (total $n!$) following the law of combination. To eliminate the ambiguity, there are some feasible methods, such as adding a third projection plane, setting a reference point outside the detecting instrument, building extra detectors for coincidence measurement, and so on.

Beyond the above-mentioned methods, we would like to solve the problem from inside the pixel sensor. This is why we propose to design *Topmetal-CEE* specially optimized for the CEE project [19]. Figure 2 shows the conceptual design of the detecting system enabled by *Topmetal-CEE*. The major innovation compared to what is discussed in Section 2.1 is the *time sensitive region* integrated with the chip. This region has excellent timing ability (better than 1 μ s) and reasonable position resolution (depending on the pixel size,

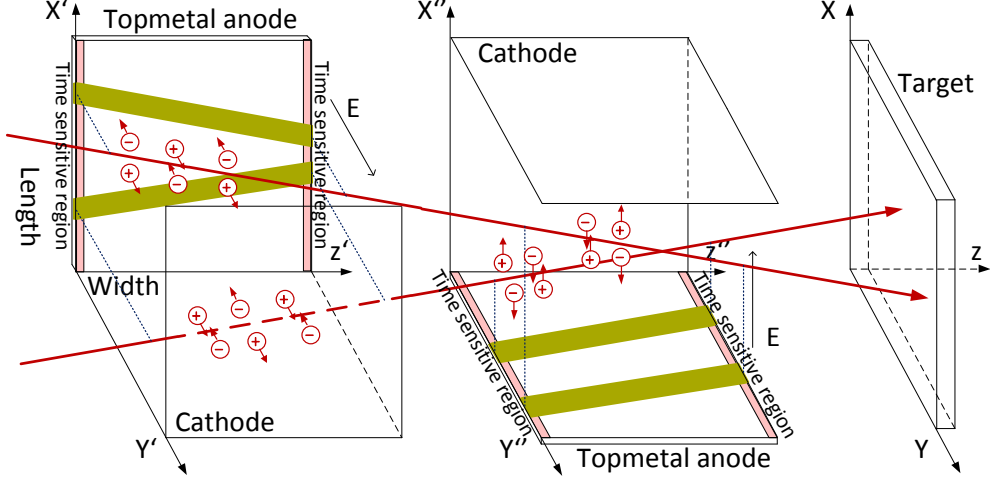


Figure 2: A conceptual design of the multi-track measurement system enabled by the *Topmetal-CEE* pixel sensor. This figure shows two incoming particles and their ionization track projections onto the *Topmetal-CEE* chip. The *Topmetal-CEE* provides position & amplitude information (the square area) and time information (the time sensitive region).

usually $\sim 100 \mu\text{m}$). When a high energy ion passes through the drift chamber, the drifting charges will trigger the time sensitive region on both sides of the pixel sensor. The timing information is thus recorded and buffered inside the chip. At fixed intervals, the recorded times are read out and used to match the tracks projecting on different coordinate planes.

In Figure 3, we plot a typical timeline of the readout scheme. Valid ions will come cross all four time sensitive regions, so their directions have a relatively small angle with regard to the z -axis in Figure 2. The main complexities arise from the row-major order of the rolling-shutter readout. We assume synchronization is maintained between the two pixel sensors, and the spatial and amplitude readout is reset at periodical slots (only the read pointer is reset, not the signals). Since the locations of the incoming ions are completely random, it is possible to receive the track projection in the current interval but read out in the next interval (x - z plane in Figure 3). As a result, the times read out in a slot might correspond to a track projection in the following interval; besides, the same ion might project on the two coordinate planes in two consecutive intervals. In spite of these complexities, in most cases the spatial and amplitude readout can match the times recorded by the time sensitive regions, and times between two coordinate plane can build up a solid relation according to the kinetics of the high energy ion. We

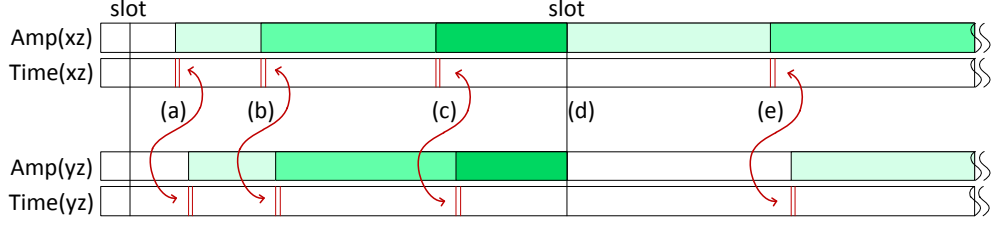


Figure 3: The timeline of the readout scheme. (a) The first ion enters the detection area and leaves tracks on the x-z plane and the y-z plane, and the crossing times are recorded by time sensitive regions of *Topmetal-CEE* so as to match the tracks. (b) The second ion enters the detection area and the tracks overlie the previous; however it is still distinguishable because recorded times by two planes can be matched. (c) The third ion enters, and it is beyond the subsequent shutters of the x-z plane while remaining in the subsequent shutters of the y-z plane; besides, times are recorded. (d) At the slot, recorded times are read out, and the shutters are reset. (e) The next ion enters, and the track overlies the previous on the x-z plane.

only need to enlarge the time-space matching region in a single pixel sensor from the current interval to consecutive two intervals, and keep the two pixel sensors synchronize. As long as the multi-track location and orientation in a single image is accurate enough, the detecting system has the capability to reconstruct 3D tracks in pile-up situations. Since the final track location and orientation is obtained by the information-rich heat-map of the projection images, results with high precision can be achieved.

Another issue needed to be explained here is the possibility of partial track images due to the rolling-shutter readout. For one thing, as stated in the previous paragraph, the direction of the valid ion has a relatively small angle with regard to the z-axis, so the probability of partial tracks is not high considering the row-major readout in the whole period. For another, if a partial track does happen in the current interval, by carefully designing the discharge circuit in each pixel, we can control the discharge time to be approximately (and optimally) one period. As a result, the partial image will become whole in the next interval, and tracks already read out will significantly dissipate. If the partial track is not evident enough to be read out in the current interval, there will be a high probability to catch the whole track in the next interval. Although switching to global-shutter readout or using multiple parallel output buffers might be more robust solutions, we believe the proposed scheme can fix the issue of partial tracks in most cases.

In the following sections, the size of the pixel array is 72×72 , and the

pixel pitch is $83.2\text{ }\mu\text{m}$, which is the *Topmetal-II*- specification and used as a reference for *Topmetal-CEE* in the conceptual design. In two-dimensional images within the subsequent sections, if not specified, the horizontal axis and the vertical axis represent indexes of the pixels. The same method is applicable to other reasonable sizes in the proper experimental condition.

3. Empirical Methods and Their Limitations

3.1. Mass Center Method

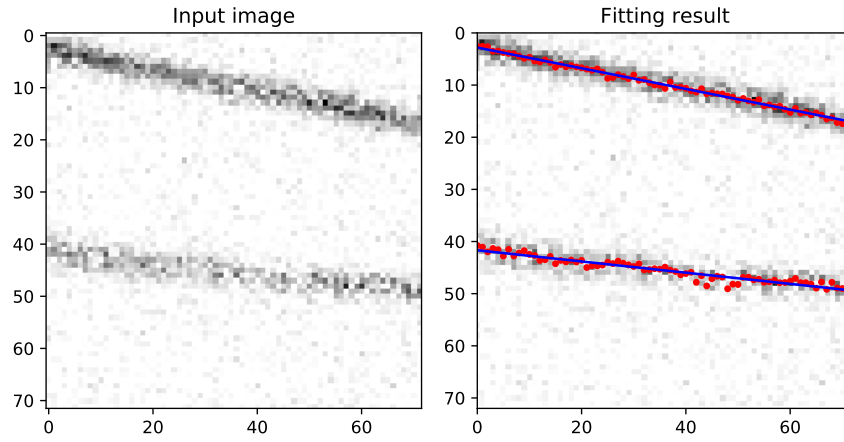


Figure 4: Location and orientation with the mass center method. (left) There are two tracks on the input image. (right) We manually separate the upper part of the image and the lower part of the image, and use the mass center method individually.

In the ideal condition (the ion path is a straight line, and ionization charges distribute evenly), the center line of the track images could represent the projection of the traversing path. *Topmetal* is a device collecting charges. Each pixel electrode collects drifting electrons and charges the capacitor. Then it is read out in the form of voltage and digitized. To take advantage of the amplitude readout of *Topmetal*, in [18] the *mass center method* is used to fit the position and direction of the tracks, which is illustrated in Figure 4. When there is only one track in the fitting region, the fitting procedure is listed as follows:

1. Process the projection image in the column-major order, and find the pixel with maximum amplitude in that column as the reference point.

2. Take 5 pixels above and below the reference point. If the number of pixels is less than 5, then take symmetrical pixels as many as possible.
3. Calculate the mass center of the pixels around the reference point (The mass of each pixel is its amplitude).
4. Fit a straight line according to the mass center of each column. The intercept and the slope represent the initial position and the direction, respectively.

The mass center method is based on the assumption of the symmetrical charge distribution, and takes advantage of amplitude readout of the hybrid pixel sensor. It is used in practice successfully. When the diffusion of the electron cloud is not so significant, the efficiency of the charge collection is relatively high and the integrity of projection tracks is guaranteed, the mass center method has good accuracy.

3.2. Double Edge Detection Method

Different from the mass center method which utilizes the intensity of the input image, the *double edge detection method* works with the contrast in the edge locations. Since the electron cloud forms patterns with a certain width on the image sensor, there are obvious changes of the intensity at the two edges of the strip. With the practical edge detection algorithm [20], we can find the two straight edges, and the center line of the two edges can represent the direct projection of the traversing path of the high energy ion. Details are listed as follows:

1. Process the input image with the Canny edge detection algorithm.
2. Perform Hough transform of the edge image after the Canny algorithm, and find the distance and angle of the edge lines in the Hough space.
3. Match the distance and angle of edge lines so as to get the number of tracks.
4. Select the center line of each matched pair as the projection of the traversing path. The intercept and the slope of the center line represent the initial position and the direction, respectively.

The double edge detection method mainly uses the features of edges on the track projection image. Its computations are based on the image after the edge detection algorithm. When the structures of the tracks are integral and multiple tracks are far away at a certain distance, the double edge detection method could detect multiple tracks and give the information of each track separately.

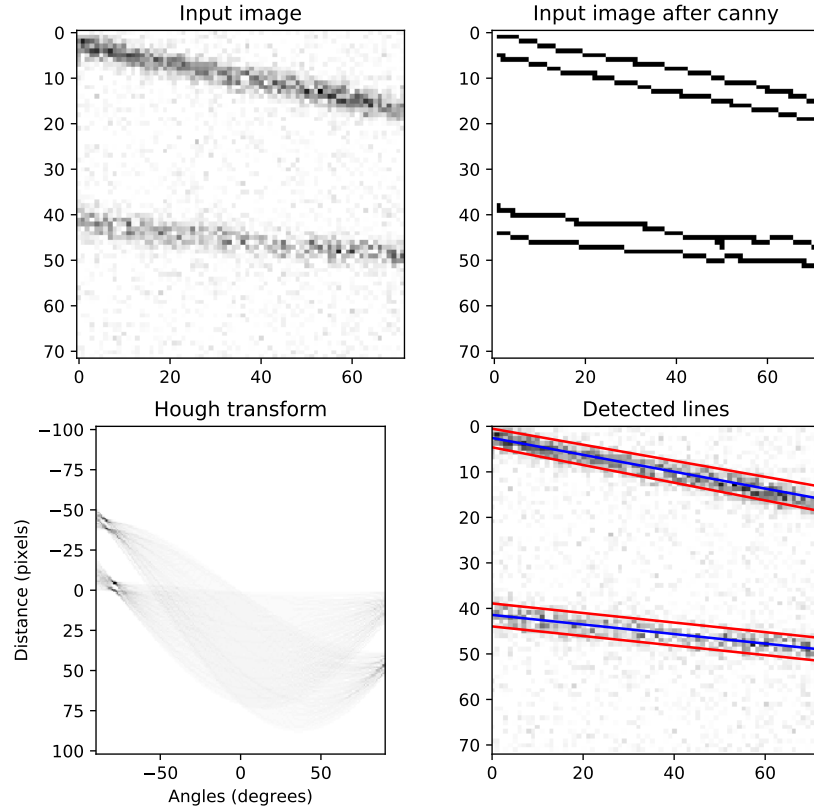


Figure 5: Location and orientation with the double edge detection method. (left top) The input image is the same as Figure 4. (right top) Canny edge detection algorithm is applied to the input image. (left bottom) Hough transform converts the edge image to the Hough space. (right bottom) Straight lines in the Hough space are matched, and the center line of each matched pair is regarded as the projection of the traversing path.

3.3. Limitations of Empirical Methods

The above two empirical methods could achieve satisfactory results in proper conditions. However, some issues with these methods are hard to resolve in practice. Here we make a discussion about the limitations of each method.

Mass Center Method. The original algorithm of the mass center method targets the single track case. When there are multiple tracks on the projection image, the mass center algorithm simply calculates the location of the mass center and does not have the ability to infer the number of tracks. If there is an error in the number, large deviations will make the results invalid. This is especially true when there are 3 or more tracks on the projection image. Furthermore, even if we can design an effective rule to judge the number of tracks before mass center calculation, the amplitude of two tracks will interplay at the overlapping regions. If we could not separate the amplitude of two or more tracks, the calculation of the mass center could not proceed correctly, which will inevitable impact on the final precision. The core problem of the mass center method is that it operates in the spatial domain and could not handle the complicated situations when tracks affect each other.

Double Edge Detection Method. For the double edge detection method, the biggest practical issue is how to determine the parameters in the algorithm. First, the Canny algorithm needs to set the standard deviation and thresholds for the Gaussian filters. This step is relatively robust and not so parameter-sensitive. Second, the Hough transform requires the divisions of the distance and the angle. If the number of divisions is too small, the "pixel" in the Hough space would be too large and it will lower the precision of the Hough transform. If the number of divisions is too large, Hough space will be more fine-grained; however, the accumulations in each "pixel" of the Hough space will decrease, and too many "pixels" with similar accumulations will make it harder to perform non-maximum suppression (NMS). Third, in the process of NMS, there are three key parameters needed to be set: minimum distance, minimum angle and threshold. If these parameters are not chosen properly, either some edges will be missed, or pseudo edges will present in the result. Finally, the core difficulty of the issue is that we want to deal with a dataset of images, or images continuously acquired from the detecting instrument. The best parameters for an image might not be suitable for another image. If

we cannot adapt the parameters to each image, the recognition rates and precision will shrink without doubt. For this reason, the double edge detection method is not a good choice for automatic streams of image data.

Finally as a supplement, these two methods belong to empirical methods based on some prior assumptions of the ideal conditions. In the physical simulation and the experiment, the physical process has its complexity, which implies that conditions out of those assumptions will happen. Once they happen, empirical methods are hard to handle them. For example, if there is a "bright point" in the projection image due to the abnormal status of the pixel sensor, the mass center method will treat it as the reference point, and it will definitely influence the position of the mass center. In conclusion, empirical methods have their safe regions and behave inadequately to account for real-world complexities.

4. Architecture

According to the analysis in Section 3, empirical methods use fixed routines to infer the position and the direction of tracks. They cannot utilize the information in the image thoroughly and cannot handle multiple tracks in a single image reliably. By contrast, deep learning techniques based on convolutional neural networks (CNN) could extract features from the input data at different levels. At the front layers, shallow features (intensity, line segment, angle) could be extracted; when the network goes deep, the pixels in the feature map have increasingly large receptive fields, and the features are more abstract (pattern or instance). Due to the hierarchy of the neural networks, they can find out the underlying relations between the input data and finish advanced classification or regression tasks.

The definition of beams in high energy physics indicates that most particles in the beam have similar location and momentum. To make our neural network model work in more general scenarios, we actually consider the multi-track problem; the initial positions and directions of the particles change in a certain range. This actually raises the difficulty to obtain the information of tracks individually. In the experiments (Section 5.6), it can be seen that the same neural network model could work very well in the real-world track projection images.

In the multi-track problem, we need to judge the number of tracks from the input projection image, and measure each track accurately. It is not

only a one-to-many problem, but also an indeterminate problem. Furthermore, the principle of the beam line implies that each particle in the beam is independently and identically distributed, which means no prior knowledge about the relative locations of multiple tracks. As a result, it is impossible to use fixed output dimensions and allocate each track to a certain output dimension. Because of these difficulties, traditional CNN structures are not suitable in this problem. We need to explore new methods to discover independent modes in the projection images and possess the regression ability at the same time.

To tackle the multi-track problem, we create an end-to-end neural network based on segmentation and fitting. This section will describe the base network, the binary segmentation, the semantic segmentation with pixel assignment, and the weighted least squares fitting separately. Finally, the configurations of the overall architecture are introduced.

4.1. Base Network

The base network in the architecture is shown in Figure 6. The configuration of parameters in each layer refers to the VGG Net [21]. The base network is made up of the encoder part and the decoder part. Convolutions with kernel size 3×3 and stride 1 are used in the encoder. The SAME padding along with the unit stride implies that the size of feature maps will not change in convolution layers. The convolution and the subsequent batch normalization [22] and rectified linear unit (ReLU) activation form the Convolution Block (Conv Block). The encoder contains three stages. In the first stage, there are two successive convolution blocks, and the number of output channels is 64. In the second stage and the third stage, the feature maps will first go through a max pooling layer with window size 2×2 and stride 2. Successive convolution blocks follow with 128 output channels in the second stage and 256 output channels in the third stage. The output of the third stage will go through a similar max pooling layer and then divide into two branches. Each branch has three successive convolution blocks. We name them the binary segmentation branch and the semantic segmentation branch in the subsequent decoder part.

In the decoder part, deconvolutions are used. If we denote the convolution operation with the matrix multiplication of the input feature map and a sparse matrix, the deconvolution can be viewed as the matrix multiplication of the output feature map and the transpose of the sparse matrix. The deconvolutions have kernel size 4×4 , stride 2 and SAME padding, so

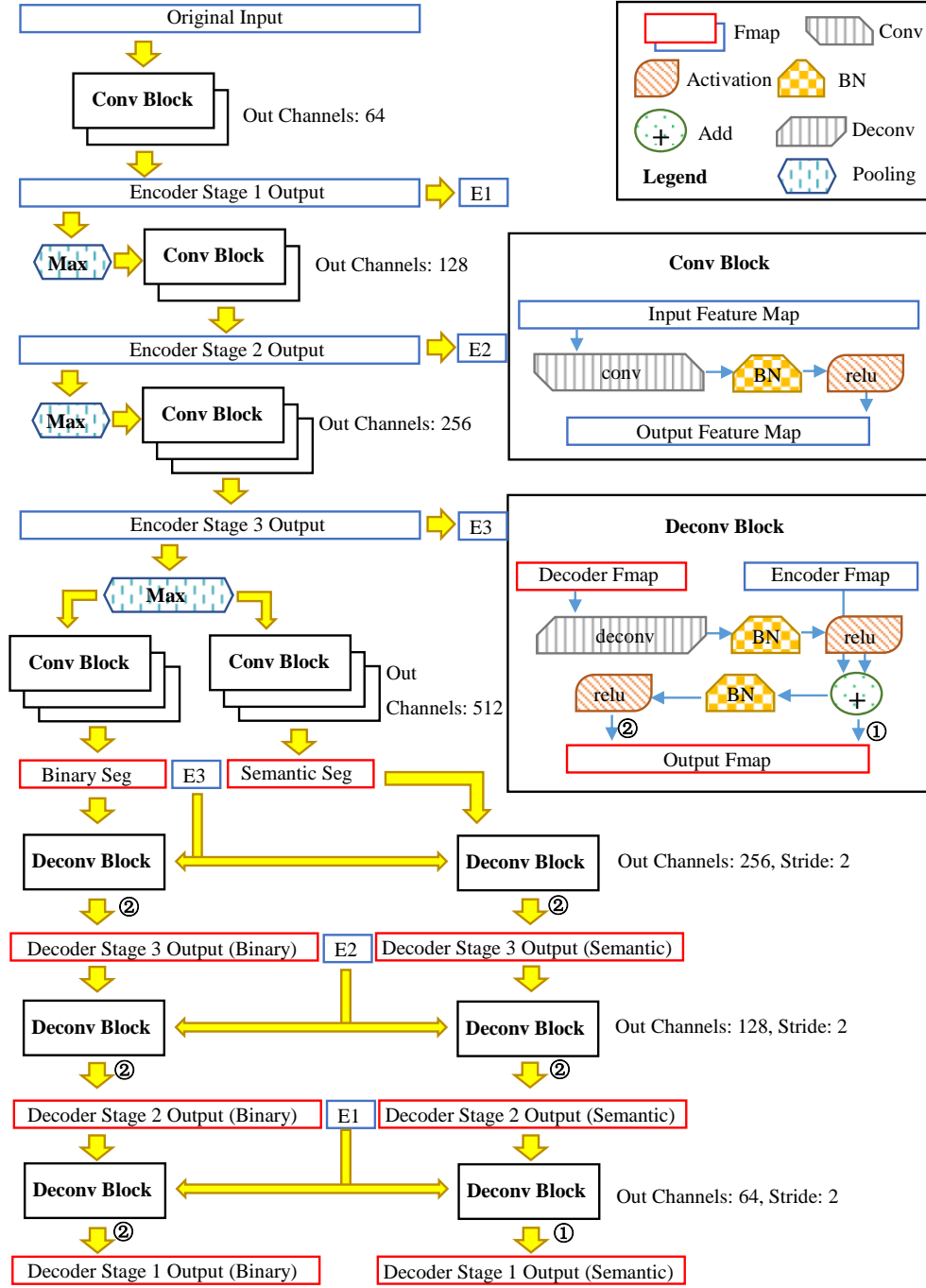


Figure 6: Base network of the propose network architecture.

the feature map is twice larger after them. The deconvolution and relevant operations form the Deconvolution Block (Deconv Block). In the deconvolution block, the feature map in the decoder will undergo deconvolution, batch normalization and ReLU; after those operations, the result is added by the corresponding feature map in the encoder, which resembles the structure in ResNet [23]. The added result can be sent out directly or after another batch normalization and ReLU. The decoder has three stages with reverse sequence numbering. The binary segmentation branch and the semantic segmentation branch share the encoder and have their own decoder layers. The output channels in the decoder correspond to the encoder (256, 128, 64). All deconvolution blocks output from ② except the last stage in the semantic segmentation branch.

4.2. Binary Segmentation

In deep learning and computer vision, the binary segmentation usually refers to generating a feature map with the same size as the original input; each pixel on the feature map could be 0 or 1 so as to discriminate a single class or a single instance. In our multi-track problem, we generalize the concept to also include the heat-map before argmax operation to get the binary map.

For the single-track case, the function of the binary segmentation is to determine the center line of the track to facilitate Hough transform; besides, we could use the heat-map before binarization to make a weighted least squares fitting. For the multi-track case, the binary result could also be used for coarse location and orientation through Hough transform; or we can combine the heat-map with the semantic segmentation and assign each pixel to different tracks. After that, weighted least squares fitting could be performed to provide accurate information of multiple tracks.

The flow diagram of the binary segmentation process is shown in Figure 7. The binary segmentation output in the base network has 64 channels. To fit into the two binary classes, a convolution layer with kernel size 1×1 and stride 1 is used to match the number of channels. In the test phase, argmax can be computed upon the convolution.

In the training phase, a label image for the binary segmentation is sent into the network and converted to the one-hot format. Since the label classes are extremely unbalanced (only the center line of each track is marked with "1"), original cross entropy loss will be biased towards backgrounds. Hence it is necessary to set larger weights for the "1" class to cancel the bias. To

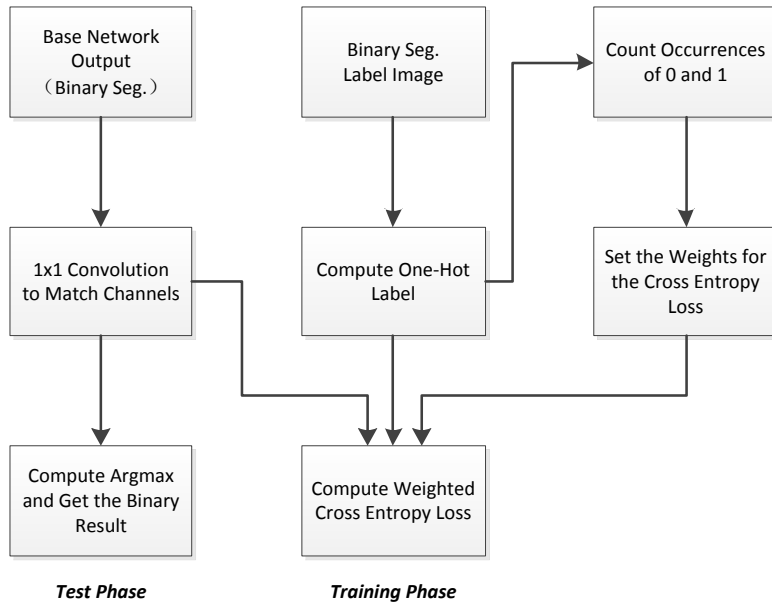


Figure 7: The flow diagram of the binary segmentation process. Input: the binary segmentation branch in the base network and the binary label image. Output: the binary segmentation result in the test phase, or the weighted cross entropy loss in the training phase.

achieve this, we count the occurrences of "0" and "1" in a minibatch and set the weights inversely correlated with the frequency:

$$w_i = \frac{1}{\log(\frac{N_i}{\sum_j N_j} + \epsilon)} \quad (1)$$

where N_i is the number of occurrences of class i , and ϵ is a positive number slightly bigger than 1 (we set it to 1.02), and w_i is the weight for class i .

To calculate the weighted cross entropy, softmax is applied to the dimension of channel in the feature map after 1×1 convolution. Then the following loss is computed:

$$\text{softmax}(\mathbf{x})_i = \frac{\exp(x_i)}{\sum_{j=1}^n \exp(x_j)} \quad (2)$$

$$L = - \sum_{m,n} \sum_i \mathbf{1}(y = i) \cdot w_i \log(\text{softmax}(\mathbf{x}_{m,n})_i) \quad (3)$$

where $\mathbf{x}_{m,n}$ is the vector at (m, n) in the feature map, softmax is computed along the vector. $\mathbf{1}(\cdot)$ is the indicative function which takes 1 when the condition is satisfied, and 0 otherwise. The binary segmentation branch can be trained with the weighted cross entropy loss by back-propagation.

4.3. Semantic Segmentation with Pixel Assignment

In computer vision, the semantic segmentation usually refers to classifying the pixels in an image according to its class property. In our multi-track problem, the task for the semantic segmentation and the following pixel assignment is to assign the pixels of the heat-map to the most appropriate tracks so as to use the weighted least squares fitting for accurate location and orientation.

Unlike what is normally considered, the semantic segmentation in our multi-track problem is to divide the pixels according to relative locations. To be more specific, we classify each pixel to one of five kinds of status: *Off*, *On*, *Up*, *Down* and *Both*. The method in detail is shown in Figure 8. In the training phase of semantic segmentation, we set label image related to the track projection image to optimize the network parameters. In the test phase, the status of each pixel is predicted. Before the weighted least squares fitting, we use operators inside the deep learning framework to assign pixels in the heat-map to proper tracks according to the results of semantic segmentation.

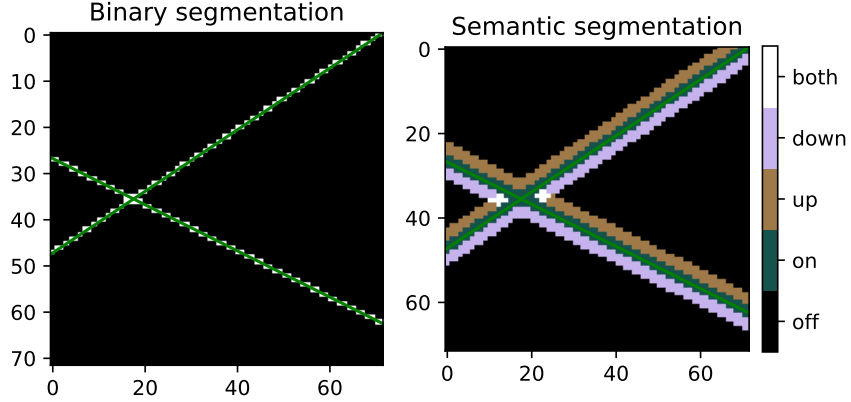


Figure 8: An example to show how binary segmentation and semantic segmentation work. We set the angles of tracks with regard to the horizontal axis more obvious than reality for better visualization. (left) Binary segmentation gives the center lines of tracks as well as a heat-map for weights in the least squares fitting. (right) Semantic segmentation annotates each pixel to one of five relative locations, and the pixel assignment uses the annotations and the Hough transform of the binary map to assign pixels to proper tracks. After that, weighted least squares fitting can be performed.

The flow diagram of the semantic segmentation process is shown in Figure 9. The diagram is similar to Figure 7, except for the following facts: (1) batch normalization and ReLU are used before 1×1 convolution; (2) Output the convolution results directly and leave the remaining work to pixel assignment; and (3) the number of matched channels or the classes increase from 2 to 5. When computing the weighted cross entropy loss, we still use Equation (1), Equation (2) and Equation (3). The only difference is the number of channels.

The pixel assignment process combines the binary segmentation and the semantic segmentation for the purpose of weighted least squares fitting, which is shown in Figure 10. The first step is to map the results of binary segmentation to the Hough space to roughly judge the number and location of tracks. In order to implement the Hough transform inside the deep learning framework, the following element-wise matrix multiplication is used:

$$H(d, \theta) = \sum_{m,n} C(m, n, d, \theta) \cdot P(m, n) \quad (4)$$

where C represents the conversion matrix of the Hough transform, P is the

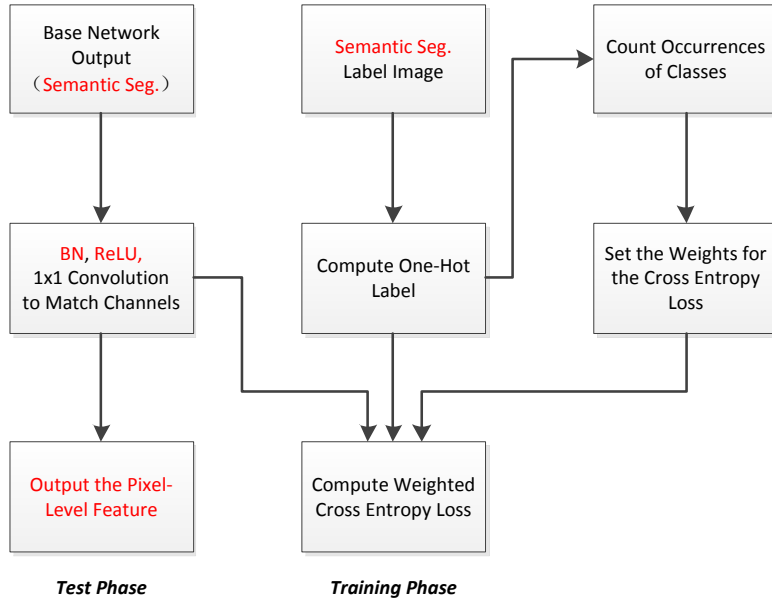


Figure 9: The flow diagram of the semantic segmentation process. Input: the semantic segmentation branch in the base network and the semantic label image. Output: the pixel-level semantic feature in the test phase, or the weighted cross entropy loss in the training phase.

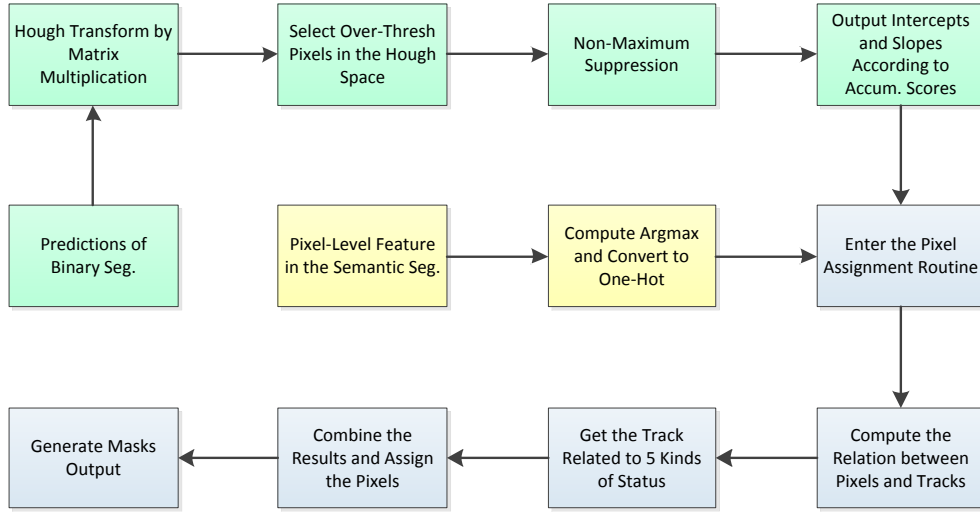


Figure 10: The flow diagram of the pixel assignment process. The green squares represent computations with the binary segmentation branch, the yellow squares with the semantic segmentation branch, and the blue squares with the pixel assignment routine. In the pixel assignment routine, relations between each pixel and each center line of the track are computed. One pixel is assigned to 0-2 tracks according to predictions of the semantic segmentation.

binary map and H is the result of the Hough transform.

Next, we select the significant regions in the Hough space by setting a threshold to half the maximum accumulations, and invoke the NMS afterwards. The outputs of NMS are converted into (intercept, slope) pairs, sorted according to the intercepts, and sent to the pixel assignment routine. On the other hand, argmax is applied to the pixel-level feature of semantic segmentation, and the one-hot results are also transferred to the pixel assignment routine.

In the pixel assignment routine, we compute the following arguments of extrema:

$$d(i, m, n) = k_i \cdot m - n + b_i \quad (5)$$

$$\text{nn}(m, n) = \arg \min_i d(i, m, n) \quad s.t. \quad d(i, m, n) \geq 0 \quad (6)$$

$$\text{pos}(m, n) = \arg \min_i d(i, m, n) \quad s.t. \quad d(i, m, n) > 0 \quad (7)$$

$$\text{np}(m, n) = \arg \max_i d(i, m, n) \quad s.t. \quad d(i, m, n) \leq 0 \quad (8)$$

$$\text{abs}(m, n) = \arg \min_i |d(i, m, n)| \quad (9)$$

where k_i represents slope, b_i represents intercept, and d represents the vertical distance between point (m,n) and the i -th track center line. nn, pos, np and abs represent the track indexes of the nearest non-negative, the nearest positive, the nearest non-positive and the nearest absolute with regard to point (m,n). If no tracks satisfy the constraints, the value will be -1 (invalid). Then, the masks are generated as follows:

$$\text{mask}(i, m, n) = \begin{cases} 1, & \text{if } \text{abs}(m, n) = i \text{ and } I(m, n, 1) = 1 \\ 1, & \text{if } \text{nn}(m, n) = i \text{ and } I(m, n, 2) = 1 \\ 1, & \text{if } \text{np}(m, n) = i \text{ and } I(m, n, 3) = 1 \\ 1, & \text{if } (\text{pos}(m, n) = i \text{ or } \text{np}(m, n) = i) \text{ and } I(m, n, 4) = 1 \\ 0, & \text{otherwise} \end{cases} \quad (10)$$

where I represents the one-hot predictions of semantic segmentation, and the mask represents the assigned pixels corresponding to each track.

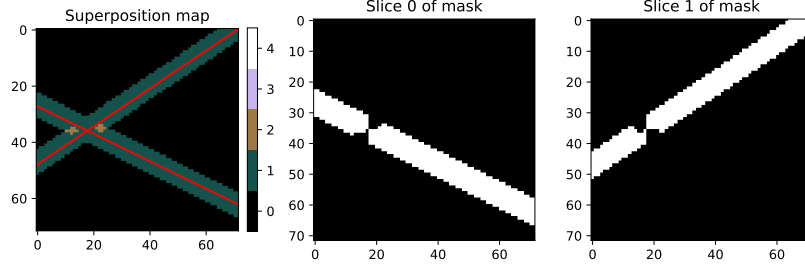


Figure 11: The pixel assignment based on the binary segmentation and semantic segmentation in Figure 8. (left) Superposition map of all the assigned pixels. (center) The pixels assigned to the first track. (right) The pixels assigned to the second track.

The example of the pixel assignment is shown in Figure 11. It can be seen that for most pixels the two tracks are discriminated very well. At the intersection of the two tracks, there will be a "gap" because of the mutual effect in the pixel assignment. However, it is not significant when we take the overall integrity into consideration. In the training phase, weighted least squares fitting is performed and the residuals are back-propagated. The optimization process ensures that the representative features are learned and the negative effect of the "gap" is reduced.

4.4. Weighted Least Squares Fitting and Its Back-Propagation

With the pixel assignment results, we can use the heat-map before binarization to make a weighted least squares fitting. Consider the following system of linear equations:

$$\mathbf{X}\boldsymbol{\beta} = \mathbf{Y} \quad (11)$$

$$\text{where } \mathbf{X} = \begin{pmatrix} 1 & x_1 \\ 1 & x_2 \\ \vdots & \vdots \\ 1 & x_m \end{pmatrix}, \quad \boldsymbol{\beta} = \begin{pmatrix} \beta_1 \\ \beta_2 \end{pmatrix}, \quad \mathbf{Y} = \begin{pmatrix} y_1 \\ y_2 \\ \vdots \\ y_m \end{pmatrix}$$

where x_i and y_i are the abscissa and the ordinate of the i -th pixel involved in the fitting, and β_i is the i -th parameter to be fitted. Usually $m \gg 2$, so the above linear equations are over-determined and no unique solution exists in the common case. To achieve the best solution, the following optimization

problem needs to be solved:

$$\boldsymbol{\beta} = \arg \min_{\mathbf{Z} \in \mathbb{R}^{2 \times 1}} \|\mathbf{X}\mathbf{Z} - \mathbf{Y}\| \quad (12)$$

There exists an analytical solution (pseudo-inverse matrix) to the optimization problem:

$$\boldsymbol{\beta} = (\mathbf{X}^T \mathbf{X})^{-1} \mathbf{X}^T \mathbf{Y} \quad (13)$$

In principle, we can apply Equation (13) directly to the non-zero pixels on the binary map to solve for the parameters. However, this method can only utilize the "0" and "1" of each pixel and not exploit the information thoroughly. Besides, it is not helpful to back-propagate through the binary segmentation branch. Therefore, we use the *weighted least squares fitting* and introduce the weights into Equation (11):

$$\mathbf{W}\mathbf{X}\boldsymbol{\beta} = \mathbf{W}\mathbf{Y} \quad (14)$$

$$\text{where } \mathbf{W} = \text{diag}(w_1, w_2, \dots, w_m) = \begin{pmatrix} w_1 & \cdots & 0 \\ \vdots & \ddots & \vdots \\ 0 & \cdots & w_m \end{pmatrix}$$

w_i is the amplitude of the i -th pixel before the binarization in the binary segmentation branch. As a result, the equation to solve for the fitting parameters becomes:

$$\boldsymbol{\beta} = ((\mathbf{W}\mathbf{X})^T \mathbf{W}\mathbf{X})^{-1} (\mathbf{W}\mathbf{X})^T \mathbf{W}\mathbf{Y} \quad (15)$$

For each track, we generate (pixel, weight) pairs after the pixel assignment. The weighted least squares of multiple tracks can be computed together in the deep learning framework and it improves the efficiency to a great extent.

To judge the accuracy of least squares fitting, we need to define the loss function. An intuitive method is to use the square errors between the fitting parameters and the label. However, the impacts of the intercept and the slope have different scales, and they work together as a whole. To separate

them manually is inappropriate. Hence, we define the geometric loss function as follows:

$$L = \sum_{x=0}^{W-1} \left[(\beta_2 x + \beta_1) - (\hat{\beta}_2 x + \hat{\beta}_1) \right]^2 \quad (16)$$

where β_1 and β_2 are predictions by the weighted least squares fitting, $\hat{\beta}_2$ and $\hat{\beta}_1$ are ground-truth values in the label, and W is the width of the image.

According to Equation (16), it is very convenient to compute the partial derivatives of the loss with regard to the fitting parameters. The core problem is how to propagate the errors to the binary segmentation branch. In Equation (15), the matrix manipulations are differentiable [24], so we can use the derivation method in the linear algebra to compute the derivatives of β with regard to W . Through Cholesky decomposition and other available methods, the derivation can be implemented in the deep learning frameworks. So far, we have cleared the last barrier of back-propagation. The constructed end-to-end model can be optimized as a whole.

4.5. Overall Architecture and Configurations

The network comprised of the base network, the binary segmentation branch and the semantic segmentation branch is shown in Figure 12. This architecture is mainly designed for images with multiple and variable tracks, and is flexible with different configurations.

Table 2: Different configurations of the network and their application scenarios.

Configuration	Network Part	Output	Loss Function	App. Scenario
Conf (1)	Base Network Binary Seg.	Hough Out Single LS Out	Binary Seg. Loss	Single Track (Coarse)
Conf (2)	Base Network Binary Seg.	Hough Out Single LS Out	Binary Seg. Loss Single LS Loss	Single Track (Precise)
Conf (3)	Base Network Binary Seg. Semantic Seg.	Hough Out LS Out	Binary Seg. Loss Semantic Seg. Loss	Multiple Tracks (Not End-to-End)
Conf (4)	Base Network Binary Seg. Semantic Seg.	Hough Out LS Out	Binary Seg. Loss Semantic Seg. Loss LS Loss	Multiple Tracks (End-to-End)

Table 2 summarizes four common configurations and their application scenarios. Conf (1) and Conf (2) are used for the single-track case, while Conf (3) and Conf (4) are used for the multi-track case. Compared to Conf (1), Conf (2) adds the single-track least squares (LS) loss, which provides

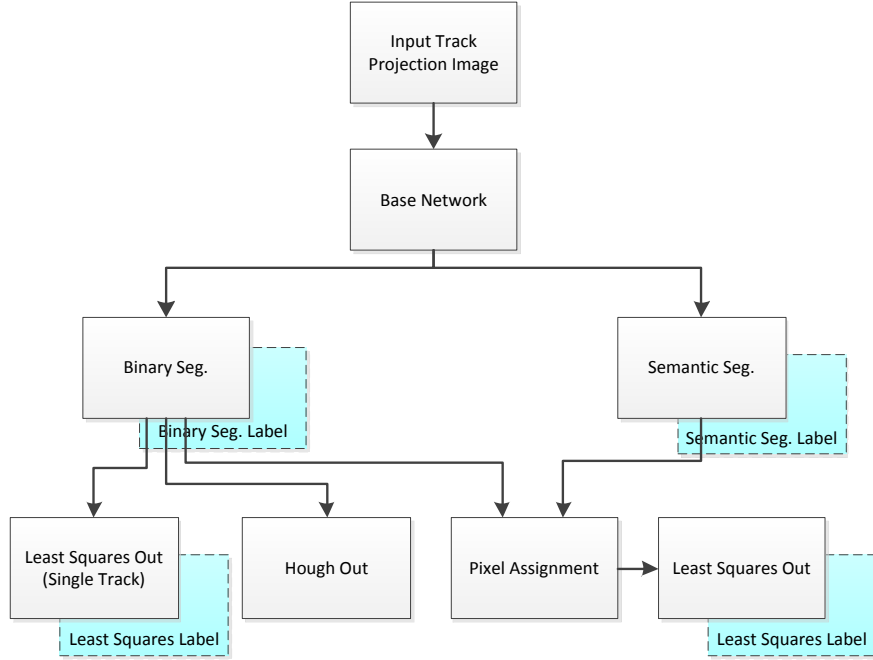


Figure 12: The overall architecture of the proposed network model. The shaded squares mean the labels working as the reference when training. The labels of least squares fitting are optional and can be discarded at the first stage of training; however, they are vital for end-to-end optimization. For the single-track, pixel assignment is not necessary for least squares fitting. For the multi-track, pixel assignment combines the two branches and provides the mask for each track.

the information of the single track with higher precision. Conf (3) and Conf (4) use the whole network including the semantic part. In Conf (3), no LS loss is used, but the LS output can still give meaningful results. Compared to Conf (3), LS loss is used in Conf (4), which makes it a fully end-to-end model.

5. Simulation and Experimental Results

5.1. Physical Simulation

To simulate the track projection images in real conditions and provide a basis for comparison between empirical methods and the neural network, we use Garfield++ [25], ROOT [26] and other software to produce high energy ion events. The whole process from the injection of ions to the collection of ionization electrons is simulated. The parameters for the detector are set according to [18]. Because we mainly discuss the location and orientation of tracks in projection images, only one projection plane with the pixel sensor is considered for simplicity.

The first step of the simulation is to generate configuration files related to the physical process. We use SRIM [27] to compute the statistical characteristics of GeV (giga electron volts) ions (Kr with 85.9 relative atomic mass in this simulation) passing through the air. The air is represented by gas mixtures of 76% N₂, 23% O₂ and 1% Ar. The computed characteristics include energy loss rate, projected range and longitudinal/lateral straggling. They provide information for the passage of the ion and ionization along the passage. Next, we use Magboltz integrated into the Garfield++ to compute the gas table in the air with identical mixtures at 1 atm and room temperature. The electric field (0~400 V/cm) is used for the gas table. Two configuration files are generated in this step and loaded in the following simulations with Garfield++.

The second step of the simulation is to generate the geometric structure, the electric field and the readout sensor. We adopt the geometry of the first detecting cell in Figure 2. The ions enter the detector from left to right. The ionization electrons drift under the horizontal electric field towards one side, and the *Topmetal* is located vertically. Figure 13 gives the side-view and top-view of the defined geometric structure, and the possible ranges of the tracks. In the side-view, the height and length of *Topmetal* are both 6 mm, and its horizontal distance to the reference point (Ref Point) is 6 mm. In the top-view, the distance from the center of the ionization region to the

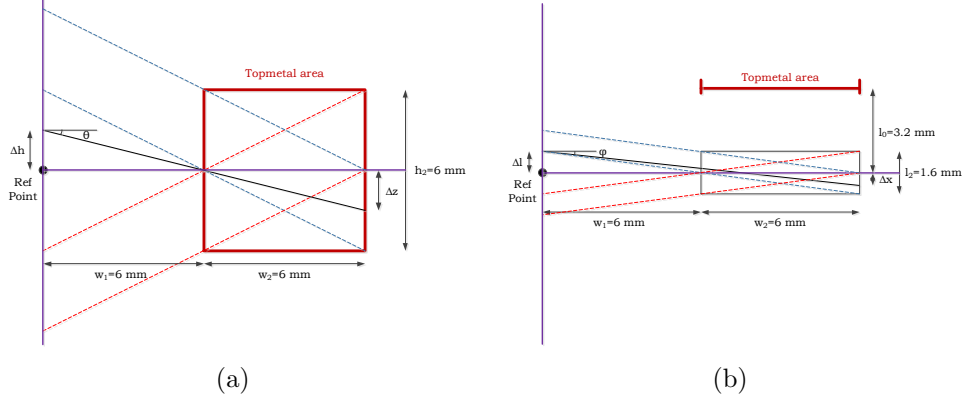


Figure 13: The geometric structure defined in the Garfield++. The *Topmetal* is placed vertically in the x-z coordinate plane, and ionization electrons drift along the y-axis. (a) A side-view of the detector geometry. (b) A top-view of the detector geometry.

Topmetal plane is 3.2 mm. We define a uniform electric field (250 V/cm) between the *Topmetal* anode (0 V) and the metal board cathode (-575 V). The *Topmetal* plane is set to be the readout sensor. When electrons reach the plane, they will leave the detecting area. The location of pixel readout is where the electrons leave.

The third step of the simulation is to generate the path of ions and ionization clusters. The energy of the Kr ion is fixed at 2.0087 GeV. The W value (average energy loss for a single ionization electron) is 30 eV [28], and the Fano factor is set to 0.3. The average atomic mass ratio (average Z/A) is set to 0.49919. To improve the efficiency of numerical computation, the ionization electrons appear in clusters, and the average number of electrons in a cluster is 500. When generating tracks, the initial position and angle should be specified. We use a stratified sampling strategy: the angle is divided into many equal ranges, and equal number of examples is generated in each range. In each range, the accurate angle obeys the uniform distribution, and the possible range of initial position is constrained by the angle. Finally, the accurate initial position is sampled from the uniform distribution. This stratified sampling strategy could ensure the coverage of different angles, which is vital to train robust models. After determining the initial kinetics of the ion, we generate tracks and associated clusters of electrons in the framework of Garfield++. These events are saved to a ROOT file to be used in the next step.

The final step of the simulation is to drift the electrons to the detecting plane, then collected by *Topmetal*. The physical parameters are the same as the former two steps. The electron collection efficiency is defined as 0.11~0.14. For electrons in the clusters, we drift them one by one to get the end-state locations. The process of drifting is implemented inside the Garfield++ to account for lateral diffusion and longitudinal diffusion. For each event, we randomly select an efficiency sampled by uniform distribution, and each electron is collected or discarded according to this probability. For collected electrons, we fill them into a two-dimensional histogram as the track projection image. The histograms and related track information are saved as a ROOT file for preprocessing in the next section.

5.2. Data Preprocessing

In the preprocessing stage, we consider the digital readout of the *Topmetal* sensor, and generate input images and label data/images for the neural network model.

When producing images for the input, we define *foreground* to be tracks in the physical simulation, and *background* to be noise intrinsic in each pixel. The histogram of collected electrons is randomly picked from the ROOT file in the previous section. Then the count of electrons is converted to sampling values of analog-to-digital converters (ADC) at 16.76 electrons per unit. Multiple histograms are summed in the foreground and converted to sampling values together to generate images with multiple and variable tracks. To avoid the same foreground image being synthesized twice in the training and test dataset, we record the indexes of each generated foregrounds and drop the combination if there is a duplication. For background, we do statistics of experimental image data at extremely low event rates. According to statistical results, we sample the noise of each pixel from the Gaussian distribution with -0.695 mean and 1.701 standard deviation. Finally, the foreground and background are added together for the final input image.

It should be noted that ADC sampling values are usual discrete by nature; however, the values on the generated input image are continuous. In practice, the projection images from experiments are also continuous because of a different mechanism. In experiments, the *pedestal* of each pixel is estimated by the average of ADC sampling values in a time span without any events; the ADC sampling values will rise and fall in a small range, so the average is continuous and varies from pixel to pixel. The actual value when events

come is the the difference between the observed value and the pedestal, so it is also continuous.

To produce labels for the binary segmentation and semantic segmentation, we take out the intercept and slope along with the histogram. A necessary step is to convert the coordinate system from physical simulation to the convention of images. Based on single-track or multi-track, the straight lines can be only one or several. For binary segmentation, we process the label image column by column, and set the pixel nearest to each straight line to value "1", otherwise value "0". For semantic segmentation, the label image is also processed in the order of columns. First, for 3 points nearest to each straight line in each column, we mark them *On*. The upper 3 points and lower 3 points with regard to *On* are candidates of *Up* and *Down*. If a point is both *Up* and *Down* candidates for different straight lines, we mark it *Both* in priority. The remaining candidates are marked as *Up* or *Down*. Finally, other points in the semantic label image are marked as *Off*. If the points are close to the edge of the image, out-of-range points are not marked.

When the above preprocessing work is done, we save the input image, the binary label image and the semantic label image to files along with the intercept and slope of each track. Besides, indexes used in each example (from the ROOT file) are also saved.

5.3. Configurations

For single-track and multi-track simulations, we use 10,000 examples for the training dataset and 2,000 examples for the test dataset. The L2 loss is used for regularization. We choose the stochastic gradient descent with momentum as the optimization algorithm. The initial learning rate and the momentum coefficient are set to 0.0001 (except for 0.000005 in the multi-track end-to-end finetuning) and 0.9. The batch size is 4 in single-track and not end-to-end conditions. When training the end-to-end neural network for multi-track with least squares loss, the batch size is 1. At different stages, we train from randomly initialized weights or on the basis of former weights (discussed in following sections). The variance scaling initializer [29] is used for weights in the convolution layers. For weights in deconvolution layers, we compute a standard deviation according to the number of input channels, and truncated normal initializer (dropping samples out of two sigma) is used with 0 mean and this standard deviation. The biases in convolution layers and deconvolution layers are initialized to 0. We stop training and test our model on the test dataset when the total loss has decreased substantially.

The network model is implemented with the TensorFlow [30] software on a desktop computer with NVIDIA GeForce TITAN X GPU (12 GB).

5.4. Single-Track Simulation

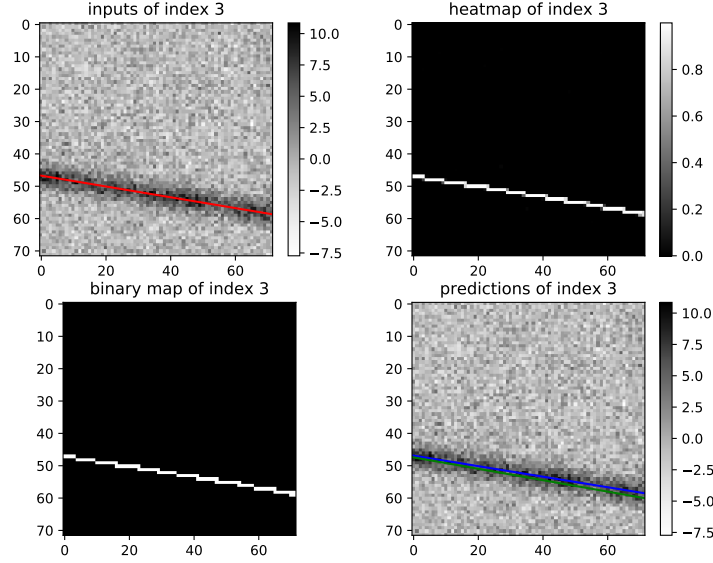


Figure 14: An example of images at different stages of the neural network model for the single-track simulation. (left top) The original input with the label (red line). (right top) The heat-map before binarization in the binary segmentation branch. (left bottom) The binary map. (right bottom) Predictions of the neural network model (blue line: weighted least squares fitting; green line: Hough output).

For the single-track simulation dataset, we create the network architecture described in Section 4 for training and testing, and compare the results with the traditional empirical methods in Section 3. We use the base network and the binary segmentation part (Conf (1) and Conf (2) in Table 2). Based on the heat-map before binarization, we make a weighted least squares fitting. First, we do not back-propagate through the least squares loss and perform relevant training and testing. Then the least squares loss is used to finetune the whole network and testing is conducted after finetuning.

In figure 14, we give an example showing how the network model deals with the single-track image. The left top image is the original input image,

Table 3: The statistics of residuals of intercept and slope predictions. For the single-track image, five methods are analyzed. The spatial resolution is estimated based on the pixel size of the *Topmetal-II*- chip in [16].

Method	Residual of Intercept			Residual of Slope		
	mean	std.	resolution (μm)	mean	std.	resolution (degree)
double edge detection	0.17711	0.62096	51.664	0.00009	0.00828	0.474
mass center	-0.00656	0.17119	14.243	0.00017	0.00393	0.225
Hough output	0.58766	0.41500	34.528	0.00018	0.01002	0.574
least squares (w/o loss)	-0.01342	0.11147	9.274	-0.00002	0.00278	0.159
least squares (w/ loss)	-0.00087	0.10559	8.785	0.00000	0.00260	0.149

Table 4: Statistics of center measure, angle measure and CAM. For the single-track image, six methods are analyzed.

Method	Center Measure	Angle Measure	CAM
double edge detection	0.9849 ± 0.0069	0.9961 ± 0.0030	0.9811 ± 0.0077
mass center	0.9984 ± 0.0034	0.9985 ± 0.0018	0.9970 ± 0.0045
Hough output (original)	0.9938 ± 0.0072	0.9951 ± 0.0033	0.9790 ± 0.0080
Hough output (adjusted)	0.9941 ± 0.0042	0.9951 ± 0.0033	0.9892 ± 0.0052
least squares (w/o loss)	0.9988 ± 0.0010	0.9987 ± 0.0011	0.9975 ± 0.0016
least squares (w/ loss)	0.9989 ± 0.0009	0.9988 ± 0.0010	0.9977 ± 0.0014

the red line in which indicates the label. After the feature extraction of the base network and binary segmentation, heat-map before binarization is shown in the right top image. It can be seen in the image that the amplitudes of pixels are highly centralized; most pixels have values close to zero, and only pixels on the center line of the track have values close to one. In the left bottom binary map, the features become even clearer. In the right bottom image, we draw the input track image again and give the results from least squares fitting (blue line) and Hough transform (green line). In total, the outputs of the neural network are approaching the label closely. It demonstrates the effectiveness of the proposed network architecture. By carefully examining the results, we can see a small shift (mainly the intercept) of the Hough transform output compared to the label. This non-ideal phenomenon is due to the discrete Hough space. In Table 4, we add an adjustment to the Hough output to correct the shift and give the results before and after the adjustment.

To quantify the performance of different methods, based on the intercept and slope predictions on the test dataset, we fit the residuals (difference from label) to a Gaussian distribution and list the mean and standard deviation (std.) in Table 3. The mean values represent the system bias of different methods, which could be greatly reduced by adding/subtracting a constant. The standard deviation could represent the resolution achieved by

the method, which is also listed beside the standard deviation. We exclude some outliers when doing statistics of the double edge detection method. For the intercept, the order of performance from bad to good is: double edge detection, Hough output, mass center, least squares (w/o loss) and least squares (w/ loss). For the slope, the double edge detection is better than the Hough output, and others are the same. It can be seen that the results from the least squares are better than the mass center in the single-track case, and the least squares (w/ loss) is slightly better than least squares (w/o loss). This demonstrates the effectiveness of the least squares method and its back-propagation. When using the least squares (w/ loss), the resolution for the initial position (intercept) and angle (slope) could be 8.785 μm and 0.149°, which is the best achievable result.

In the above analysis, we deal with the initial position and angle separately. However, they are two sides of a single problem and cannot be totally isolated. To quantify the precision in a systematic way, we introduce the *center-angle measure* (CAM) which combines both the location and orientation:

$$c = 1 - \frac{\|\mathbf{C}_{label} - \mathbf{C}_{pred}\|_2}{0.5 \cdot L_{label}} \quad (17)$$

$$a = 1 - \frac{|\theta_{label} - \theta_{pred}|}{90^\circ} \quad (18)$$

$$CAM = c \cdot a \quad (19)$$

where \mathbf{C}_{label} and \mathbf{C}_{pred} represent the center positions of the label line segment and the predicted line segment. We calculate the L2 distance between the two centers and divide it by half the length of the label. θ_{label} and θ_{pred} represent the angles of the label line and the predicted line. We calculate the absolute difference between the two angles and divide it by 90 degrees. The center positions and angles are calculated from intercepts and slopes generated by different methods and recorded in the label. The product of the center measure and angle measure is defined as the CAM.

In Table 4, we gather the results of center measure, angle measure and CAM using different methods. The mean and standard deviation are calculated on the test dataset. Comparing the final CAM, the order of performance from bad to good is: Hough output (original), double edge detection, Hough output (adjusted), mass center, least squares (w/o loss) and least squares

(w/ loss). It is consistent with the results in Table 3. The CAM achieved by least squares (w/ loss) could be 0.9977 ± 0.0014 and indicates superior precision. In comparison, the CAM of the mass center could be 0.9970 ± 0.0045 , which has smaller mean value and much larger fluctuations.

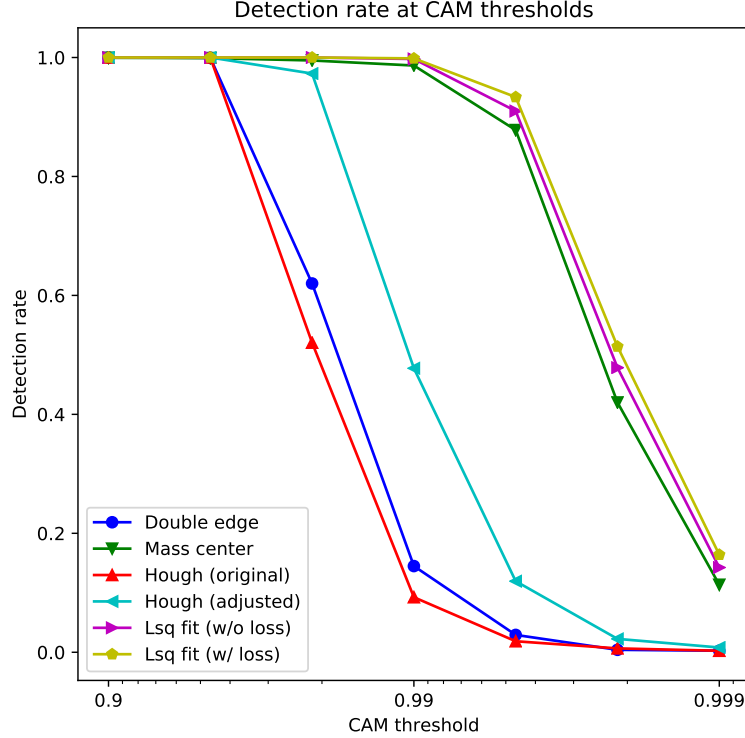


Figure 15: Detection rates of different methods versus the CAM threshold for the single-track image. At a specific threshold, the test results with CAM above the threshold are considered as detected. We use the logarithmic x-axis in the figure.

In Figure 15, we compare the detection rates of different methods at CAM thresholds. The detection rate refers to the ratio of tested images above a CAM threshold. The scale of the x-axis is logarithmic from 0.9 to 0.999. It can be seen that the overall trend of the curves is in good accordance with Table 4. The difference between the mass center and least squares is not large. However, the advantage of least squares is still noticeable, and the relative improvement is more evident at high CAM thresholds.

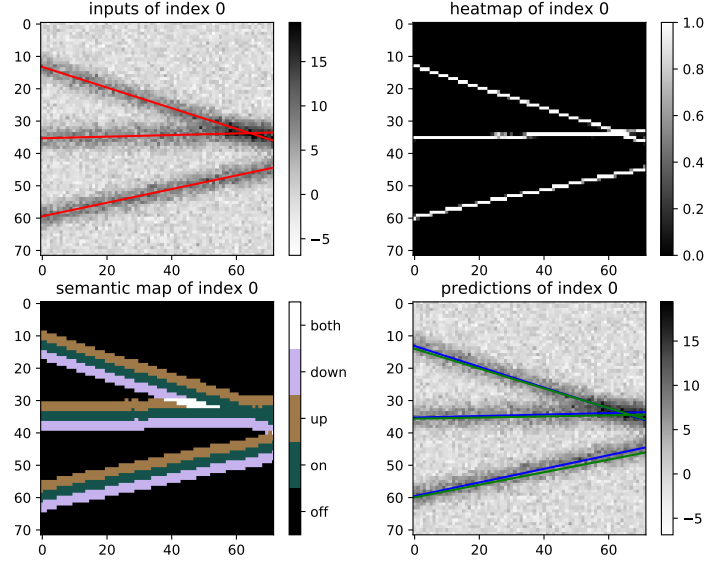


Figure 16: An example of images at different stages of the neural network model for the multi-track simulation. (left top) The original input with the label (red line). (right top) The heat-map before binarization in the binary segmentation branch. (left bottom) The result of semantic segmentation. (right bottom) Predictions of the neural network model (blue line: weighted least squares fitting; green line: Hough output).

Table 5: The statistics of residuals of intercept and slope predictions. For the multi-track image, three methods are analyzed. The upper part uses 1-3 tracks, and the lower part uses 1-5 tracks. The spatial resolution is estimated based on the pixel size of the *Topmetal-II*- chip in [16].

Method	Residual of Intercept			Residual of Slope		
	mean	std.	resolution (μm)	mean	std.	resolution (degree)
Hough output	0.61478	0.43175	35.922	0.00001	0.01036	0.594
least squares (w/o loss)	0.01227	0.15250	12.688	0.00022	0.00403	0.231
least squares (w/ loss)	0.00419	0.13722	11.417	0.00003	0.00366	0.210
Hough output	0.60142	0.44297	36.855	-0.00014	0.01086	0.622
least squares (w/o loss)	0.00916	0.19269	16.032	0.00047	0.00553	0.317
least squares (w/ loss)	-0.01206	0.18281	15.210	0.00011	0.00504	0.289

Table 6: Statistics of center measure, angle measure and CAM. For the multi-track image, four methods are analyzed. The upper part uses 1-3 tracks, and the lower part uses 1-5 tracks.

Method	Center Measure	Angle Measure	CAM
Hough output (original)	0.9833 ± 0.0075	0.9949 ± 0.0035	0.9783 ± 0.0081
Hough output (adjusted)	0.9939 ± 0.0044	0.9949 ± 0.0035	0.9888 ± 0.0056
least squares (w/o loss)	0.9983 ± 0.0018	0.9983 ± 0.0017	0.9966 ± 0.0030
least squares (w/ loss)	0.9985 ± 0.0016	0.9984 ± 0.0016	0.9968 ± 0.0026
Hough output (original)	0.9836 ± 0.0077	0.9947 ± 0.0040	0.9784 ± 0.0087
Hough output (adjusted)	0.9936 ± 0.0048	0.9948 ± 0.0038	0.9884 ± 0.0064
least squares (w/o loss)	0.9977 ± 0.0033	0.9977 ± 0.0028	0.9954 ± 0.0054
least squares (w/ loss)	0.9979 ± 0.0030	0.9979 ± 0.0026	0.9958 ± 0.0050

5.5. Multi-Track Simulation

For the multi-track simulation dataset, we create the full network architecture comprised of the base network, binary segmentation and semantic segmentation (Conf (3) and Conf (4) in Table 2). First, training and testing are performed without the least squares loss. Next, the loss is used to finetune the network end-to-end, and testing is conducted again after finetuning.

In Figure 16, we give an example visualizing different stages of the network. The left bottom image is the result from semantic segmentation, and other images and their annotations are the same as Figure 14. The multi-track discrimination is more difficult than the single-track case. In this example, two tracks are close to each other, and intersect at the right edge of the input image. In the right top heat-map, the intersecting region is somewhat vague; however, the "X" shape is well distinguishable. In the left bottom image, there are also some non-ideal pixels, but the overall condition is fairly good. The network predictions in the right bottom image are approaching the label. Again, the Hough output (green line) has a shift compared to the weighted least squares output (blue line), which could be fixed with an adjustment.

To set up relations between the predicted tracks and tracks in the label, we use a *greedy match algorithm*. First, for each example in the test dataset, we build up a CAM matrix; the numbers of rows and columns are the numbers of predicted tracks and label tracks, and the content is the CAM calculated using the prediction and the label. Each time we select the maximum element in the CAM matrix, record the relation between the row (prediction) and the column (label) and leave out the row and the column in subsequent matching. The process continues until no elements in the CAM matrix satisfying the condition.

In Table 5 and Table 6, we show the statistical results of Hough output and least squares in different conditions. Two multi-track datasets are used in this section: 1-3 tracks dataset and 1-5 tracks dataset. They are listed in the upper part and low part of the tables, respectively. For the intercept and slope, the precision of the least squares method is higher than Hough output. Compared to the least squares (w/o loss), the least squares (w/ loss) can improve the precision further. It should be noted that the resolution of initial position and angle achieved by the least squares (w/ loss) in 1-3 tracks dataset ($11.417 \mu\text{m}$ and 0.210°) is still better than mass center in the single-track dataset ($14.243 \mu\text{m}$ and 0.225°). It demonstrates the superiority of the network architecture. Besides, when using the 1-5 tracks dataset, the performance only deteriorates a little, and the same model is still competent in feature extraction. For CAM results, the trend is almost the same.

Finally, we give the F1-macro and F1-micro curves of different methods versus the CAM threshold. We define TP_i to be successfully matched tracks above the CAM threshold in an example, $(TP_i + FP_i)$ to be total predicted tracks in an example and $(TP_i + FN_i)$ to be total label tracks in an example. The F1-macro and F1-micro can thus be calculated:

$$P_i = \frac{TP_i}{TP_i + FP_i}, \quad R_i = \frac{TP_i}{TP_i + FN_i}, \quad F1_i = \frac{2 \cdot P_i \cdot R_i}{P_i + R_i} \quad (20)$$

$$\text{F1-macro} = \frac{1}{N} \sum_{i=1}^N F1_i \quad (21)$$

$$P = \frac{\sum_{i=1}^N TP_i}{\sum_{i=1}^N (TP_i + FP_i)}, \quad R = \frac{\sum_{i=1}^N TP_i}{\sum_{i=1}^N (TP_i + FN_i)} \quad (22)$$

$$\text{F1-micro} = \frac{2 \cdot P \cdot R}{P + R} \quad (23)$$

The curves of F1-macro and F1-micro are shown in Figure 17 and Figure 18. The scale of the x-axis is logarithmic ranging from 0.9 to 0.999. It can be seen that the least squares fitting is better than Hough output in both figures, which is in good accordance with Table 6. The least squares (w/ loss) is slightly better than the least squares (w/o loss), and it is more obvious in the F1-micro figure. In two figures, we plot results of 1-3 tracks dataset

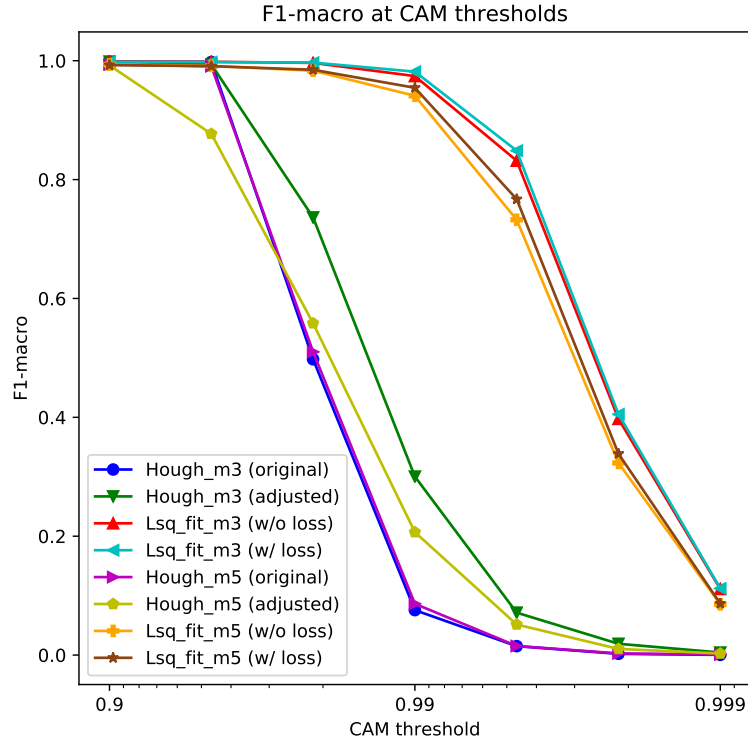


Figure 17: F1-macro of different methods versus the CAM threshold for the multi-track image. F1-macro is the average of F1 scores of individual examples. We use the logarithmic x-axis in the figure. The suffix "m3" means dataset with 1-3 tracks, and the suffix "m5" means dataset with 1-5 tracks.

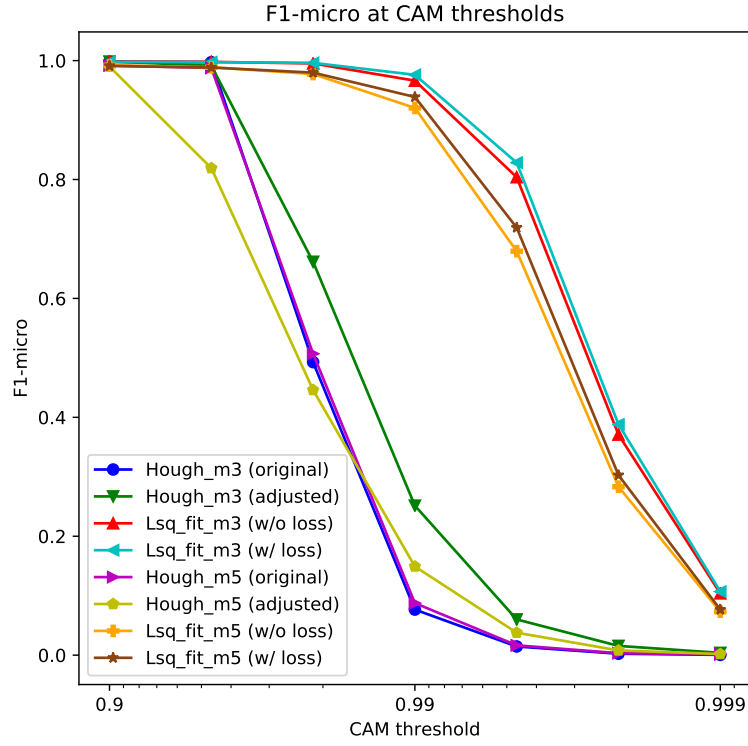


Figure 18: F1-micro of different methods versus the CAM threshold for the multi-track image. F1-micro is the F1 score of all the examples. We use the logarithmic x-axis in the figure. The suffix "m3" means dataset with 1-3 tracks, and the suffix "m5" means dataset with 1-5 tracks.

along with 1-5 tracks dataset. For the least squares, the latter results are slightly worse because of the track images are more complicated. However, the degradation of performance is acceptable. For the Hough output, we notice a drop of the Hough output (adjusted) for the 1-5 tracks dataset at low CAM thresholds. Preliminarily we attribute the drop to the greedy match algorithm we use. Besides, the performances of Hough output (original) are quite close.

5.6. Analysis of Experimental Images

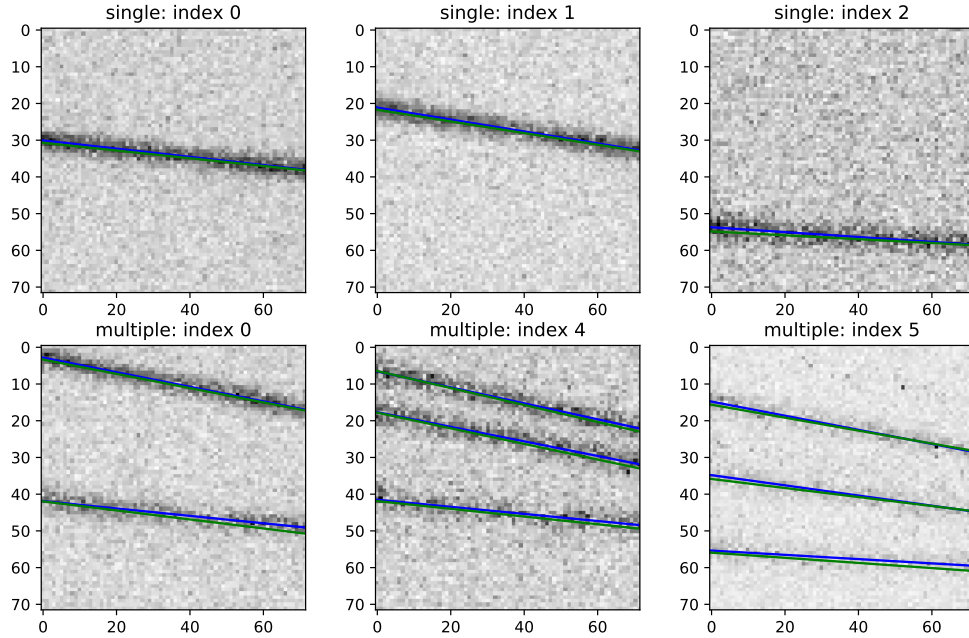


Figure 19: Test results of applying the trained network weights to experimental data. The upper three images show the single-track case, and the lower three images show the multi-track case. The predictions of least squares fitting (blue line) and Hough output (green line) are plotted.

To demonstrate the effectiveness of the proposed network architecture in experiments, we qualitatively analyze the test results with the experimental images. These images come from the experiment in [18]. We directly apply the trained network weights to initialize the model, and the results are shown in Figure 19. In these figures, the gray-scale background image is the experimental data, and the line segments are predictions of least squares fitting

(blue line) and Hough output (green line). Based on the observation of the background track images, the individual difference is considerably large. For example, in the right top image, the difference between the noisy background and the track is relatively small, which indicates the increase of amplitude on the track is not obvious; in the right bottom image, the pattern of tracks is very centralized, which may be caused by the short drifting distance of the electron cloud. In spite of these diversities and discrepancy between simulations and experiments, the weights trained with the simulation data could very well recognize the tracks in the experiment. Whether the least squares or Hough output is used, it can correctly judge the number of tracks and give the accurate position and angle. When we carefully examine the images, we find that the prediction of least squares fitting is nearer to the center line of each track. This is consistent with the previous simulations.

6. Conclusions

In this paper, we mainly discuss the multi-track location and orientation problem in the gaseous drift chamber based on the *Topmetal* series pixel sensor. First, we briefly introduce the detecting instrument used in the previous experiment and the conceptual design implemented with the newly developed *Topmetal-CEE* chip. When describing the scheme of measurement, we emphasize on the capability of multi-track detection enabled by the time & amplitude readout of the *Topmetal-CEE*.

Next, two traditional empirical methods, mass center method and double edge detection method, are introduced, and their limitations in the specific problem are thoroughly analyzed. these empirical methods and their limitations show the possibilities to improve the performance of location and orientation, and shed light on the direction to design novel deep learning methods.

The proposed architecture is an end-to-end neural network based on segmentation and fitting. It is comprised of the base network, the binary segmentation branch and the semantic segmentation branch. The base network adopts an encoder-decoder structure, and the two decoder parts share the encoder. The binary segmentation generates the heat-map for weighted least squares fitting and the binary map for Hough transform. The semantic segmentation maps each pixel to five possible relative locations, which paves the way for the following pixel assignment. Weighted least squares fitting is implemented inside the deep learning framework with full back-propagation

compatibility. The network architecture could be trained end-to-end to eliminate irretrievable errors from stage to stage.

After that, the procedures of physical simulation and data preprocessing are described in detail. In the first place, single-track simulation is performed with comparison to empirical methods. The simulation results show that the least squares method is significantly better than mass center method, and least squares with loss can improve the precision further on the basis of the trained network. In the second place, multi-track simulation is conducted with 1-3 tracks dataset and 1-5 tracks dataset. We find that the least squares method with 1-3 tracks dataset can still perform better than mass center method in the single-track case. Least squares with loss have the highest precision throughout the simulations. The location resolution could achieve 8.8 μm for the single track and 11.4 μm (15.2 μm) for the 1-3 tracks (1-5 tracks), and the orientation resolution could achieve 0.15° and 0.21° (0.29°) respectively. Finally, results on the experimental data demonstrate the robustness of the physical simulation and the validity of the method in real-world experiments.

In the future, we would like to deploy the algorithm on application-specific integrated circuits or field programmable gate arrays for on-line and on-site feature extraction. To achieve this, the optimization and quantization of the network architecture could be necessary.

Acknowledgements

This research is partly supported by the National Natural Science Foundation of China (Grant Number 11875146, U1932143), and partly supported by the National Key Research and Development Program of China (Grant Number 2016YFE0100900).

References

- [1] The ATLAS Collaboration, The ATLAS experiment at the CERN large hadron collider, Journal of Instrumentation 3 (08) (2008) S08003–S08003. doi:10.1088/1748-0221/3/08/s08003. URL <https://doi.org/10.1088/1748-0221/3/08/s08003>
- [2] Z. Wang, S. Zou, Y. Fan, J. Liu, X. Sun, D. Wang, H. Kang, D. Sun, P. Yang, H. Pei, G. Huang, N. Xu, C. Gao, L. Xiao, A beam monitor

using silicon pixel sensors for hadron therapy, Nuclear Instruments and Methods in Physics Research Section A: Accelerators, Spectrometers, Detectors and Associated Equipment 849 (2017) 20 – 24. doi:10.1016/j.nima.2016.12.050.

URL <http://www.sciencedirect.com/science/article/pii/S0168900216313183>

- [3] L. Badano, M. Benedikt, P. Bryant, M. Crescenti, P. Holy, P. Knaus, A. Maier, M. Pullia, S. Rossi, Synchrotrons for hadron therapy: Part i, Nuclear Instruments and Methods in Physics Research Section A: Accelerators, Spectrometers, Detectors and Associated Equipment 430 (2) (1999) 512 – 522. doi:10.1016/S0168-9002(99)00206-5.

URL <http://www.sciencedirect.com/science/article/pii/S0168900299002065>

- [4] Z. Xu, R. Mao, L. Duan, Q. She, Z. Hu, H. Li, Z. Lu, Q. Zhao, H. Yang, H. Su, C. Lu, R. Hu, J. Zhang, A new multi-strip ionization chamber used as online beam monitor for heavy ion therapy, Nuclear Instruments and Methods in Physics Research Section A: Accelerators, Spectrometers, Detectors and Associated Equipment 729 (2013) 895 – 899. doi:10.1016/j.nima.2013.08.069.

URL <http://www.sciencedirect.com/science/article/pii/S0168900213012102>

- [5] O. Actis, D. Meer, S. Knig, Precise on-line position measurement for particle therapy, Journal of Instrumentation 9 (12) (2014) C12037–C12037. doi:10.1088/1748-0221/9/12/c12037.

URL <https://doi.org/10.1088%2F1748-0221%2F9%2F12%2Fc12037>

- [6] R. S. Sussmann, CVD diamond for electronic devices and sensors, John Wiley & Sons, Chichester, United Kingdom, 2009. doi:10.1002/9780470740392.

- [7] M. Alvarado, A. Ayala, M. A. Ayala-Torres, W. Bietenholz, I. Dominguez, M. Fontaine, P. Gonzalez-Zamora, L. M. Montao, E. Moreno-Barbosa, M. E. P. Salazar, L. Moreno, P. Nieto-Marn, V. Reyna Ortiz, M. Rodriguez-Cahuantzi, G. Tejeda-Muoz, M. E. Tejeda-Yeomans, A. Villatoro-Tello, C. Zepeda Fernandez, A beam-beam monitoring detector for the mpd experiment at nica, Nuclear

Instruments and Methods in Physics Research Section A: Accelerators, Spectrometers, Detectors and Associated Equipment 953 (2020) 163150. doi:10.1016/j.nima.2019.163150.
 URL <http://www.sciencedirect.com/science/article/pii/S0168900219314639>

- [8] J. Son, S. Lee, Y. Lim, S. Park, K. Cho, M. Yoon, D. Shin, Development of optical fiber based measurement system for the verification of entrance dose map in pencil beam scanning proton beam, *Sensors* 18 (1) (2018) 227. doi:10.3390/s18010227.
- [9] Gianotti, Paola, The padme detector, *EPJ Web Conf.* 170 (2018) 01007. doi:10.1051/epjconf/201817001007.
 URL <https://doi.org/10.1051/epjconf/201817001007>
- [10] Y. LeCun, Y. Bengio, G. Hinton, Deep learning, *Nature* 521 (7553) (2015) 436–444. doi:10.1038/nature14539.
 URL <https://doi.org/10.1038/nature14539>
- [11] E. Shelhamer, J. Long, T. Darrell, Fully convolutional networks for semantic segmentation, *IEEE Transactions on Pattern Analysis and Machine Intelligence* 39 (4) (2017) 640–651. doi:10.1109/TPAMI.2016.2572683.
- [12] V. Badrinarayanan, A. Kendall, R. Cipolla, Segnet: A deep convolutional encoder-decoder architecture for image segmentation, *IEEE Transactions on Pattern Analysis and Machine Intelligence* 39 (12) (2017) 2481–2495. doi:10.1109/TPAMI.2016.2644615.
- [13] A. Paszke, A. Chaurasia, S. Kim, E. Culurciello, Enet: A deep neural network architecture for real-time semantic segmentation, *CoRR* abs/1606.02147. arXiv:1606.02147.
 URL <http://arxiv.org/abs/1606.02147>
- [14] D. Neven, B. D. Brabandere, S. Georgoulis, M. Proesmans, L. V. Gool, Towards end-to-end lane detection: an instance segmentation approach, in: *2018 IEEE Intelligent Vehicles Symposium (IV)*, 2018, pp. 286–291. doi:10.1109/IVS.2018.8500547.
- [15] Y. Fan, C. Gao, G. Huang, X. Li, Y. Mei, H. Pei, Q. Sun, X. Sun, D. Wang, Z. Wang, Development of a highly pixelated direct charge

sensor, topmetal-i, for ionizing radiation imaging, arXiv abs/1407.3712.
arXiv:1407.3712.
URL <http://arxiv.org/abs/1407.3712>

- [16] M. An, C. Chen, C. Gao, M. Han, R. Ji, X. Li, Y. Mei, Q. Sun, X. Sun, K. Wang, L. Xiao, P. Yang, W. Zhou, A low-noise cmos pixel direct charge sensor, topmetal-ii-, Nuclear Instruments and Methods in Physics Research Section A: Accelerators, Spectrometers, Detectors and Associated Equipment 810 (2016) 144 – 150. doi:10.1016/j.nima.2015.11.153.
URL <http://www.sciencedirect.com/science/article/pii/S0168900215015727>
- [17] C. Gao, G. Huang, X. Sun, Topmetal-II-: a direct charge sensor for high energy physics and imaging applications, Journal of Instrumentation 11 (01) (2016) C01053–C01053. doi:10.1088/1748-0221/11/01/c01053.
URL <https://doi.org/10.1088%2F1748-0221%2F11%2F01%2Fc01053>
- [18] Z. Li, Y. Fan, Z. Wang, J. Liu, X. Sun, C. Zhao, H. Pei, D. Wang, G. Huang, D. Zhang, D. Sun, P. Yang, C. Gao, L. Xiao, A new method for directly locating single-event latchups using silicon pixel sensors in a gas detector, Nuclear Instruments and Methods in Physics Research Section A: Accelerators, Spectrometers, Detectors and Associated Equipment 962 (2020) 163697. doi:10.1016/j.nima.2020.163697.
URL <http://www.sciencedirect.com/science/article/pii/S0168900220302540>
- [19] L. L, H. Yi, Z. Xiao, M. Shao, S. Zhang, G. Xiao, N. Xu, Conceptual design of the hirfl-csr external-target experiment, Science China Physics, Mechanics & Astronomy 60 (1) (2016) 012021. doi:10.1007/s11433-016-0342-x.
URL <https://doi.org/10.1007/s11433-016-0342-x>
- [20] J. Canny, A computational approach to edge detection, IEEE Transactions on Pattern Analysis and Machine Intelligence PAMI-8 (6) (1986) 679–698. doi:10.1109/TPAMI.1986.4767851.
- [21] K. Simonyan, A. Zisserman, Very deep convolutional networks for large-scale image recognition, in: 3rd International Conference on Learning

- Representations (ICLR), 2015.
URL <http://arxiv.org/abs/1409.1556>
- [22] S. Ioffe, C. Szegedy, Batch normalization: Accelerating deep network training by reducing internal covariate shift, in: Proceedings of the 32nd International Conference on International Conference on Machine Learning - Volume 37, ICML15, JMLR.org, 2015, p. 448456.
 - [23] K. He, X. Zhang, S. Ren, J. Sun, Deep residual learning for image recognition, in: 2016 IEEE Conference on Computer Vision and Pattern Recognition (CVPR), 2016, pp. 770–778. doi:10.1109/CVPR.2016.90.
 - [24] M. Giles, An extended collection of matrix derivative results for forward and reverse mode automatic differentiation, Report, University of Oxford (2008).
 - [25] H. Schindler, Microscopic simulation of particle detectors, Thesis (2012).
 - [26] R. Brun, F. Rademakers, Root an object oriented data analysis framework, Nuclear Instruments and Methods in Physics Research Section A: Accelerators, Spectrometers, Detectors and Associated Equipment 389 (1) (1997) 81 – 86, new Computing Techniques in Physics Research V. doi:10.1016/S0168-9002(97)00048-X.
URL <http://www.sciencedirect.com/science/article/pii/S016890029700048X>
 - [27] J. F. Ziegler, M. Ziegler, J. Biersack, Srim the stopping and range of ions in matter (2010), Nuclear Instruments and Methods in Physics Research Section B: Beam Interactions with Materials and Atoms 268 (11) (2010) 1818 – 1823, 19th International Conference on Ion Beam Analysis. doi:10.1016/j.nimb.2010.02.091.
URL <http://www.sciencedirect.com/science/article/pii/S0168583X10001862>
 - [28] J. M. Valentine, S. C. Curran, Average energy expenditure per ion pair in gases and gas mixtures, Reports on Progress in Physics 21 (1) (1958) 1–29. doi:10.1088/0034-4885/21/1/301.
URL <https://doi.org/10.1088%2F0034-4885%2F21%2F1%2F301>
 - [29] K. He, X. Zhang, S. Ren, J. Sun, Delving deep into rectifiers: Surpassing human-level performance on imagenet classification, in: 2015

IEEE International Conference on Computer Vision (ICCV), 2015, pp. 1026–1034. doi:10.1109/ICCV.2015.123.

- [30] M. Abadi, P. Barham, J. Chen, Z. Chen, A. Davis, J. Dean, M. Devin, S. Ghemawat, G. Irving, M. Isard, M. Kudlur, J. Levenberg, R. Monga, S. Moore, D. G. Murray, B. Steiner, P. A. Tucker, V. Vasudevan, P. Warden, M. Wicke, Y. Yu, X. Zheng, Tensorflow: A system for large-scale machine learning, in: K. Keeton, T. Roscoe (Eds.), 12th USENIX Symposium on Operating Systems Design and Implementation, OSDI 2016, Savannah, GA, USA, November 2-4, 2016, USENIX Association, 2016, pp. 265–283.

URL <https://www.usenix.org/conference/osdi16/technical-sessions/presentation/abadi>